The effects of gas diffusion layers structure on water transportation using X-ray computed tomography based Lattice Boltzmann method

Fontip Jinuntuya[a], Michael Whiteley[b], Rui Chen[b*], Ashley Fly[b]

[a]Department of Mechanical Engineering, University of Phayao, Thailand

[b]Aeronautical & Automotive Engineering, Loughborough University, United Kingdom

Highlights:

- X-ray computed tomography used to reconstruct three different types of GDL
- Models of GDLs analysed using Lattice Boltzmann method
- Invasion pattern and saturation of water in the GDLs is controlled by wettability
- Liquid water travelled with a stable displacement under hydrophilic angles
- Conversely, at hydrophobic contact angles it travelled with capillary fingering

Abstract

The Gas Diffusion Layer (GDL) of a Polymer Electrolyte Membrane Fuel Cell (PEMFC) plays a crucial role in overall cell performance. It is responsible for the dissemination of reactant gasses from the gas supply channels to the reactant sites at the Catalyst Layer (CL), and the adequate removal of product water from reactant sites back to the gas channels.

Existing research into water transport in GDLs has been simplified to 2D estimations of GDL structures or use virtual stochastic models. This work uses X-ray computed tomography (XCT) to reconstruct three types of GDL in a model. These models are then analysed via Lattice Boltzmann methods to understand the water transport behaviours under differing contact angles and pressure differences.

In this study, the three GDL samples were tested over the contact angles of 60°, 80°, 90°, 100°, 120° and 140° under applied pressure differences of 5kPa, 10kPa and 15kPa. By varying the contact angle and pressure difference, it was found that the transition between stable displacement and capillary fingering is not a gradual process. Hydrophilic contact angles in the region of $60° < \theta < 90°$ showed stable displacement properties, whereas contact angles in the region of $100° < \theta < 140°$ displayed capillary fingering characteristics.

1. Introduction

With the recent proliferation of environmentally friendly consciousness regarding energy use, various sustainable energy conversion technologies have been explored to mitigate anthropogenic climate change concerns. One such technology is the hydrogen fuel cell. When sustainably sourced H_2 is used as an input fuel, Polymer Electrolyte Membrane Fuel Cells (PEMFC) are considered to be zero-emissions energy conversion devices. Already used in commercial applications such as consumer electronics and automotive traction power units, the PEMFC has shown great promise. However, there are still areas that require improvement as to advance this promising technology; one of which is the performance of the cell.

The Gas Diffusion Layer (GDL) of a PEMFC plays a crucial role in overall performance in the form of providing unrestricted pathways for the reactant gases to be adequately transported from a gas channel in the separating plates to the Catalyst Layer (CL), allowing the initiation of the reaction. The GDL is also responsible for the removal of product water from the CL to the gas channels, and ultimately out of the cell. The excessive presence of liquid water in the GDL drastically diminishes the performance of the cell by blocking reactant gas access to active sites in the CL. To this end, GDLs are normally treated with a hydrophobic coating (Polytetrafluoroethylene (PTFE)) to ease the removal of product water from the cell.

A wide range of studies have investigated water transport within a PEMFC in recent years, however the behaviour of liquid water in the GDL at a pore-level is currently inadequately understood. Experimental methods including Nuclear Magnetic Resonance (NMR) imaging, neutron imaging, X-ray imaging, and direct optical visualisation remain difficult to fully understand at a microscopic level due to the limitations of spatial and temporal resolutions involved in such techniques [1].

Fluorescence microscopy techniques combined with conventional optical photography were used by Lister, et al. [2] to visualize through-plane liquid water transport in the GDL. Bazylak, et al. [3] from

the same research group examined the influence of cell compression on the behaviour of liquid water transport in GDL materials using the same technique, finding that certain compressed regions of the GDL provided preferential pathways for liquid water transport, leading to a breakthrough in the test apparatus. Both works showed good advancements in visualisation of liquid water behaviour in a PEMFC GDL, however their technique was limited to the visualization of liquid water transport in the upper layers of the GDL due to the opacity of the material.

Prediction of the saturation distribution of liquid water has been modelled on a macroscopic level by numerous previous studies [4-10]. These models are based on volume averaging theory and make the assumption of homogeneous GDL material. Due to this, they fail to incorporate the influence of pore morphology of the GDL material on the transportation of liquid water [11]. Furthermore, these existing models depend upon empirical relationships of capillary pressure-saturation and relative permeability-saturation in order to predict liquid water behaviour within the GDL. Capillary pressure is normally expressed as a function of saturation using the Leverett function, and therefore is more likely to harbour inaccuracies as it was based upon experimental data of homogenous soil or sand with uniform wettability. These media differ significantly when compared to a GDL structure in a PEMFC [11-13].

To model on a pore-scale rather than macro-scale, techniques such as Pore Network (PN) and Lattice Boltzmann (LB) modelling have emerged as favourable methods for simulating fluid flow through porous media. In opposition to macro-scale techniques, PN and LB methods can uncover the underlying influence of microscopic features on liquid water transportation in the GDL structure.

Numerous PN models have been used to analyse water transportation in porous media, using 2D [14-18] and 3D [19-23] domains. In such works, however, the complex structure of the GDL material is often simplified to a regular sphere [23] or cubic pores [22] that are then connected via columnar throats for 3D PNs. 2D PNs are connected via an array of randomly distributed, equal-sized disks with random diameters [14,15].

The Lattice Boltzmann method has increased in popularity in recent years, due to its capability to incorporate complex boundaries of an actual GDL material as manufactured [24, 11]. To date however, the majority of existing studies on fluid transport in GDL materials integrate artificial structures that are generated by stochastic simulation techniques [25-27]. The stochastic method uses a set of structural inputs obtained from design specifications or measured data to then reconstruct a porous medium [27]. However, this method is inadequate to fully reconstruct a GDL material sample. Another potential drawback to the use of stochastic methods is that it struggles to model the binding material that holds a GDL material together sufficiently. Many works therefore ignore the binder material altogether, resulting in an over-simplification and possibly altering the pore size and shape within the model.

For these reasons, XCT techniques have been increasingly used in this field to more accurately reconstruct the GDL material in a digital domain [28-31]. Rama et al. [24] undertook a study on the feasibility of using the combined methods of XCT and LB modelling to simulate liquid flow, at a pore scale, through PEMFC GDL materials. Their simulated results were compared to experimental results using a Frazier air tester, and their correlation error was found to be 3% greater than the measured one. This breakthrough, alongside numerous other studies [28-30], showed that XCT and LB are well suited for combination to accurately model liquid water flow through a PEMFC GDL.

Existing work by various authors shows that PEMFC GDLs have been heavily simulated using a variety of techniques to discover a wide range of results. The emerging methodology has been shown to be the use of XCT in combination with the LB method to simulate GDL water transport properties. Although existing work has looked into water flow through GDLs under differing operating conditions, there is little work in the area of differing wettability of XCT reconstructed GDLs, and this effect on water transport.

To this end, this work looks at the water transport behaviour under varying wettability conditions by using XCT reconstructed GDL models of three types of commercial GDL material. These models are then analysed using the LB method.

The GDL wettability parameters are then altered so that the effect of this change can be analysed. The wettability of a GDL sample is defined by the contact angle (θ) of liquid water with the solid surface structure of the GDL sample. Hydrophilic wettability is considered to exist between $0°<\theta<90°$, and hydrophobic wettability is considered to exist between contact angles of $90°<\theta<180°$. The GDL samples were simulated between the full range of contact angles and at pressure difference of 5kPa, 10kPa, and finally 15kPa.

2. X-Ray Reconstructed GDL Models

Three types of commercially available GDL materials were used in this study; Freudenberg H2315 felt, Toray TGP-H-120 paper and SGL 24AA paper. The GDL samples were untreated and contained no PTFE or Micro-Porous Layer (MPL) additions. All samples are similar in that they are all non-woven and are composed of multiple layers. Their inherent structure however, differs between samples. The Freudenberg felt has curved fibres travelling in both the in-plane and through-plane directions. Both the Toray and SGL papers have straight fibres which are mainly orientated in the in-plane direction. Both paper GDL fibres are held together by a carbonized binder, which differ in construction. The SGL binder has a rougher texture binder than the Toray paper, and it lies within the in-plane and through-plane directions, whereas the Toray binder is only located between layers in the in-plane direction.

Each sample was analysed through XCT processes at a resolution of 2.5 µm/pixel, and reconstructed in digital form. A General Electric Phoenix nanotom® system was used, equipped with an X-ray source of 160 kV (max) and 250 µA (max), with an X-ray spot size of around 1µm.

The detector was a 5-megapixel flat panel CMOS (complementary metal-oxide semiconductor) with a GOS (gadolinium oxysulfide) scintillator deposited on a fibre optic plate.

The results of the scans are presented in **Figure 1** alongside their 3D digital reconstructions.

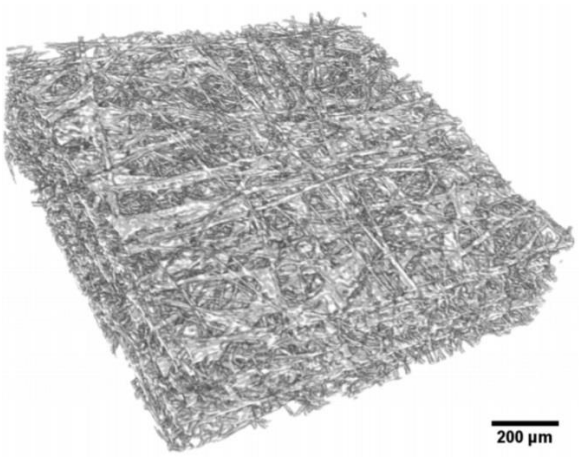

(a)

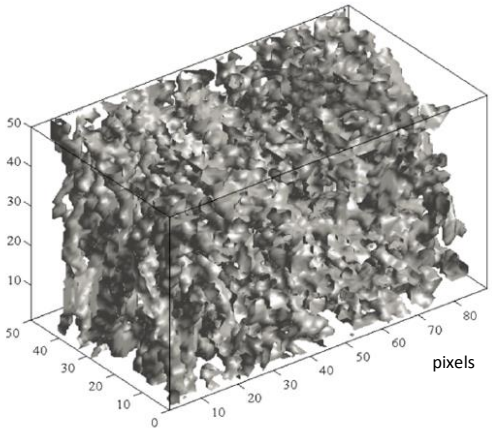

(d)

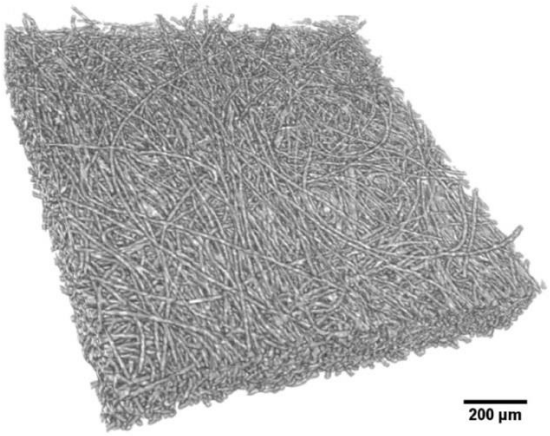

(b)

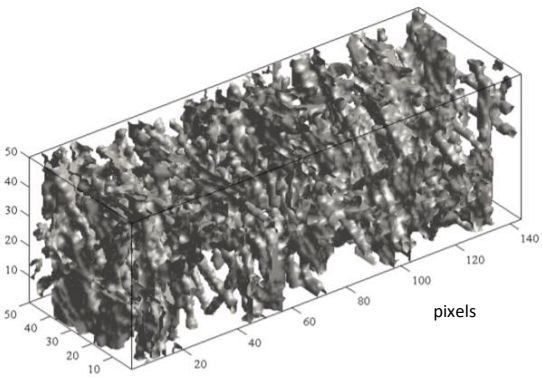

(e)

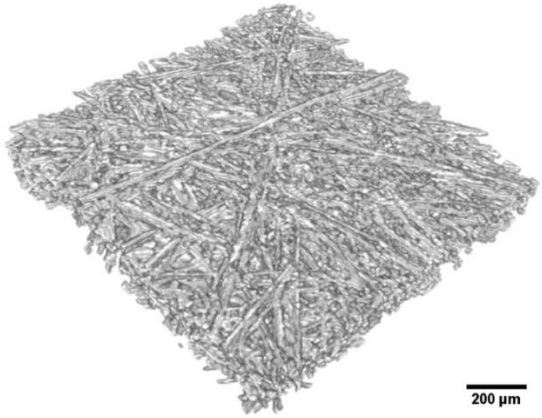

(c)

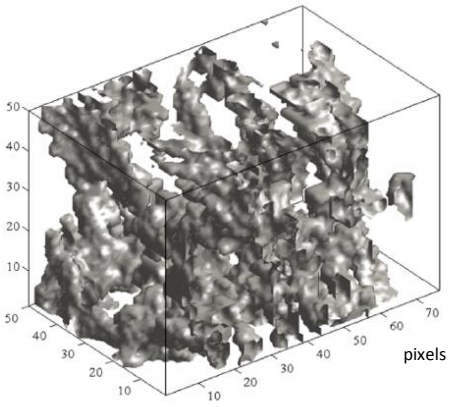

(f)

Figure 1*- 3D binary model of the Freudenberg felt, Toray paper, and SGL paper GDL samples, with their respective 3D digital representations*

3. Two-Phase Lattice Boltzmann Modelling

As discussed in Section 1, the LB method is widely used to model fluid particle flow through porous media. In this work, multiple relaxation time (MRT) LB methods were used, based upon the evolution of fluid particle distribution functions for each fluid, described in Equation 1.

$$f_{i,k}(x+\xi_i\delta t) = f_{i,k}(x,t) + \Omega^k\left[f_{i,k}^{eq}(x,t) - f_{i,k}(x,t)\right] \quad (1)$$

where $f_{i,k}(x,t)$ is the particle distribution function for fluid k at location x at time t, moving with velocity ξ_i in the ith direction, $f_{i,k}^{eq}(x,t)$ is the equilibrium distribution function for fluid k , which is the value of $f_{i,k}(x,t)$ at equilibrium state, δt is a time increment during which the particle travels from one location to another, and Ω^k is the collision matrix. In this study, a 3-dimensional model with 19 lattice velocities (D3Q19) was utilized. The equilibrium distribution functions for each fluid for the D3Q19 model are given by Equations 2 & 3.

$$f_{i,k}^{eq} = w_i\rho_k\left[1 - \frac{3}{2}u_k^{eq}\cdot u_k^{eq}\right] i = 0 \quad (2)$$

$$f_{i,k}^{eq} = w_i\rho_k\left[1 + 3\xi_i\cdot u_k^{eq} + \frac{9}{2}\left(\xi_i\cdot u_k^{eq}\right)^2 - \frac{3}{2}u_k^{eq}\cdot u_k^{eq}\right] i = 1,2,3,\ldots,18, \quad (3)$$

where w_i is a weighting factor depending on the magnitude of the velocity ξ_i ($w_i = 1/3$ for $|\xi_i| = 0$, $w_i = 1/18$ for $|\xi_i| = \delta x/\delta t$ and $w_i = 1/36$ for $|\xi_i| = 2\sqrt{\delta x/\delta t}$).

The speed of sound is given by $c_s = \frac{1}{\sqrt{3}}\delta x/\delta t$.

The equilibrium velocity u_k^{eq} for fluid k is given by [32,33]

$$\rho_k u_k^{eq} = \rho_k u' + \tau_k F_k \quad (4)$$

Where u' is the bulk fluid velocity of the two fluids, and it is calculated using:

$$u' = \frac{\sum_k \rho_k u_k/\tau_k}{\sum_k \rho_k/\tau_k} \quad (5)$$

Where ρ_k is the macroscopic density of fluid k, and is calculated from:

$$\rho_k = \sum_{i=0}^{18} f_{i,k} \quad (6)$$

And u_k is the velocity of fluid k, taken from:

$$\rho_k u_k = \sum_{i=0}^{18} \xi_i f_{i,k}\,(x,t) \quad (7)$$

The total force F_k acting on the fluid k includes the fluid-fluid interaction F_{f-f}^k and fluid-solid interaction F_{f-s}^k and is expressed using:

$$F_k = F_{f-f}^k + F_{f-s}^k \quad (8)$$

3.1 Model Validation

Model validation is required as to confirm the accuracy of the simulation in relation to real-world results. The density (ρ_a/ρ_w) and viscosity (μ_a/μ_w) ratios of water and air are 1:800 and 1:15 respectively, which is beyond the capabilities of the LB method used in this work. Such high densities used in the LB method used in this work could lead to numerical instabilities [28,29].

In order to determine whether liquid water transport through the GDL can be simulated using this technique, some non-dimensional parameters were calculated. The Bond number is representative of the ratio of gravitational force to interfacial force and is represented by:

$$Bo = g(\rho_w - \rho_a)D^2/\sigma \quad (9)$$

The capillary number defines the ratio between viscous force and interfacial force, given by:

$$Ca = \mu_a U_w/\sigma \quad (10)$$

The Reynolds number denotes the ratio between inertial force to viscous force, as presented by:

$$Re = \mu_w U_w / \sigma \quad (11)$$

The Weber number is the ratio of inertial force to interfacial force

$$We = \rho_w U_w^2 D / \sigma \quad (12)$$

From these equations, D is the average pore diameter in the GDL, g is acceleration due to gravity, U_w , ρ_w and μ_w are velocity, density and viscosities of water. Whereas ρ_a and μ_a are the densities and viscosities of air respectively. Water-to-air interfacial tension is represented by σ.

An average pore diameter of 10 µm was taken from the work in [28,29], and subsequently used in this work. Values for the Bond, capillary, Reynolds, and Weber were also taken from [29].

For a GDL in operation in a PEMFC, the three dimensionless numbers have approximate values of; 1.6×10^{-4}, $2.47 \times 10^{-8} – 1.92 \times 10^{-7}$, $1.65 \times 10^{-4} – 2.12 \times 10^{-4}$, and $4.08 \times 10^{-12} – 4.07 \times 10^{-11}$ for Bond, capillary, Reynolds and Weber numbers respectively. From these numbers it is clear that the effect of gravity is negligible with respect to the interfacial tension force. Also, the viscous force is negligible when compared to the capillary force. Likewise, the inertial force is negligible when compared to the viscous force.

To this end, the viscosity difference and large density of air and water, which in turn have an effect on inertial, gravitational and viscous forces, would seem to have very limited effect on liquid water transport in a PEMFC GDL. Thus, it is concluded from the above, that water intrusion into PEMFC GDLs is mainly controlled by capillary action.

For a two-phase LB model to accurately simulate water transport, two input variables are required. The fluid-fluid interaction strength parameter, given by $g_{k\bar{k}}$, and the fluid-solid strength parameter given by g_{ks}. $g_{k\bar{k}}$ denotes the fluid-fluid interfacial tension, whereas g_{ks} is responsible for denoting the wettability of the solid wall. These parameters are not practically measurable, and therefore a

series of numerical experiments were undertaken [28] to ascertain values. Said values were used in this study.

3.2 Simulation Boundary Setup

To simulate water transport through an initially dry GDL, a water reservoir was added to the front end of the GDL structure, and an air reservoir at the end. A difference in pressure was then introduced between the two to force water across the material in the through-plane direction. The remaining four boundaries to the model were treated as periodic boundaries, meaning that any particle leaving the domain would then return to the other side of the domain with the same properties. As discussed in section 3, a three-dimensional model with 19 velocity directions (D3Q19) was used for this simulation. The Isothermal condition is assumed for this work.

The digital reconstruction of each GDL sample is shown in **Figure 1d-f**.

Both the digital and physical dimensions of each sample is shown in **Table 1**:

Table 1 - Digital and Physical dimensions of each sample GDL

Sample	**Freudenberg H2315**	**Toray TGP-H-120**	**SGL 24AA**
Resolution (µm/pixel)	2.5	2.5	2.5
Digital size (pixel^3)	50x50x89	50x50x114	50x50x76
Physical size (µm^3)	125x125x222.5	125x125x360	125x125x190

3.3 Simulation Process

All of the GDL samples analysed using XCT methods were tested with contact angles of 60°, 80°, 90°, 100°, 120° and 140°, using applied pressure differences of 5kPa, 10kPa and 15kPa. In doing so, greater comparisons can be drawn from the effects that these variables have on water transport in each GDL sample.

The simulations were run until liquid water broke through to the air side, or until it was clear that water would not progress any further under those conditions.

4. Results and Discussion

4.1 Invasion Pattern

Figures 2-4 show the water intrusion pattern at varying stages during the simulation and at varying contact angles. The first image shows the initial stage of water intrusion, whereas the third image to the right shows the final stage, either at breakthrough or stagnation. The top row is the shallowest contact angle of 60^{o}, and the bottle row is the steepest of 140^{o}. This is shown for each pressure difference of 5 kPa, 10 kPa, and 15 kPa (a, b, and c respectively).

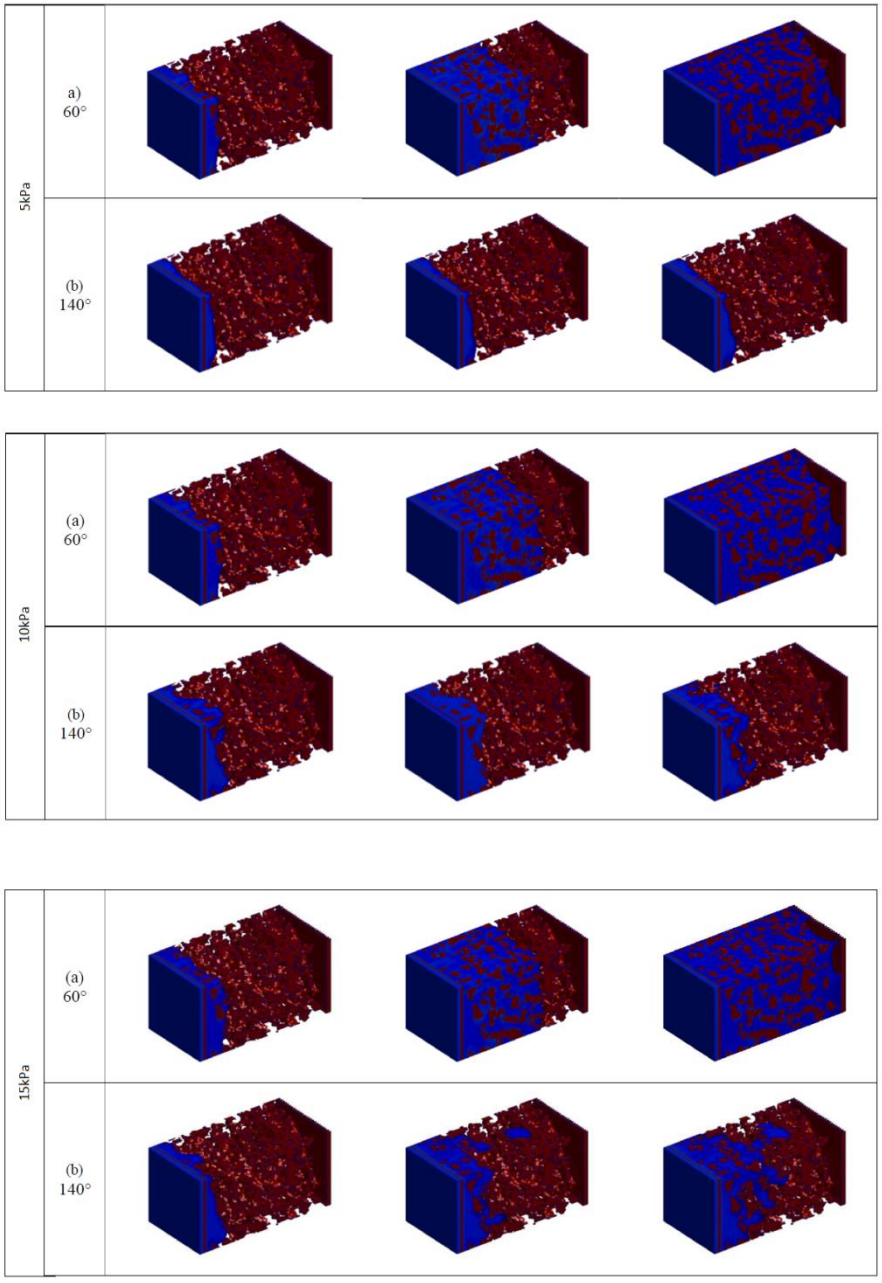

Figure 2 *- Freudenberg felt intrusion patterns at contact angle of a) 60° b) 140° under 5 kPa, 10 kPa, and 15 kPa pressure differences*

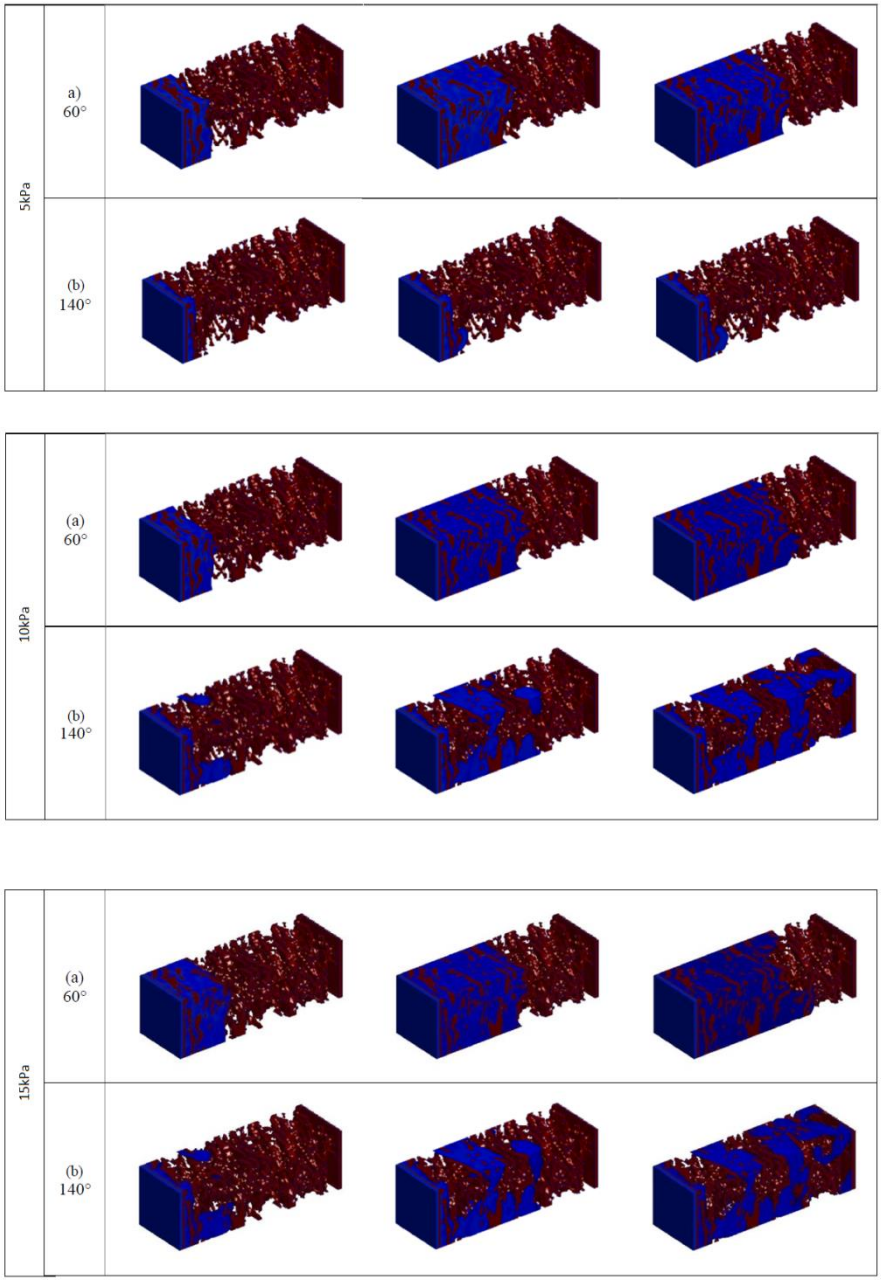

Figure 3 *- Toray paper intrusion patterns at contact angle of a) 60° b) 140° under 5 kPa, 10 kPa, and 15 kPa pressure differences*

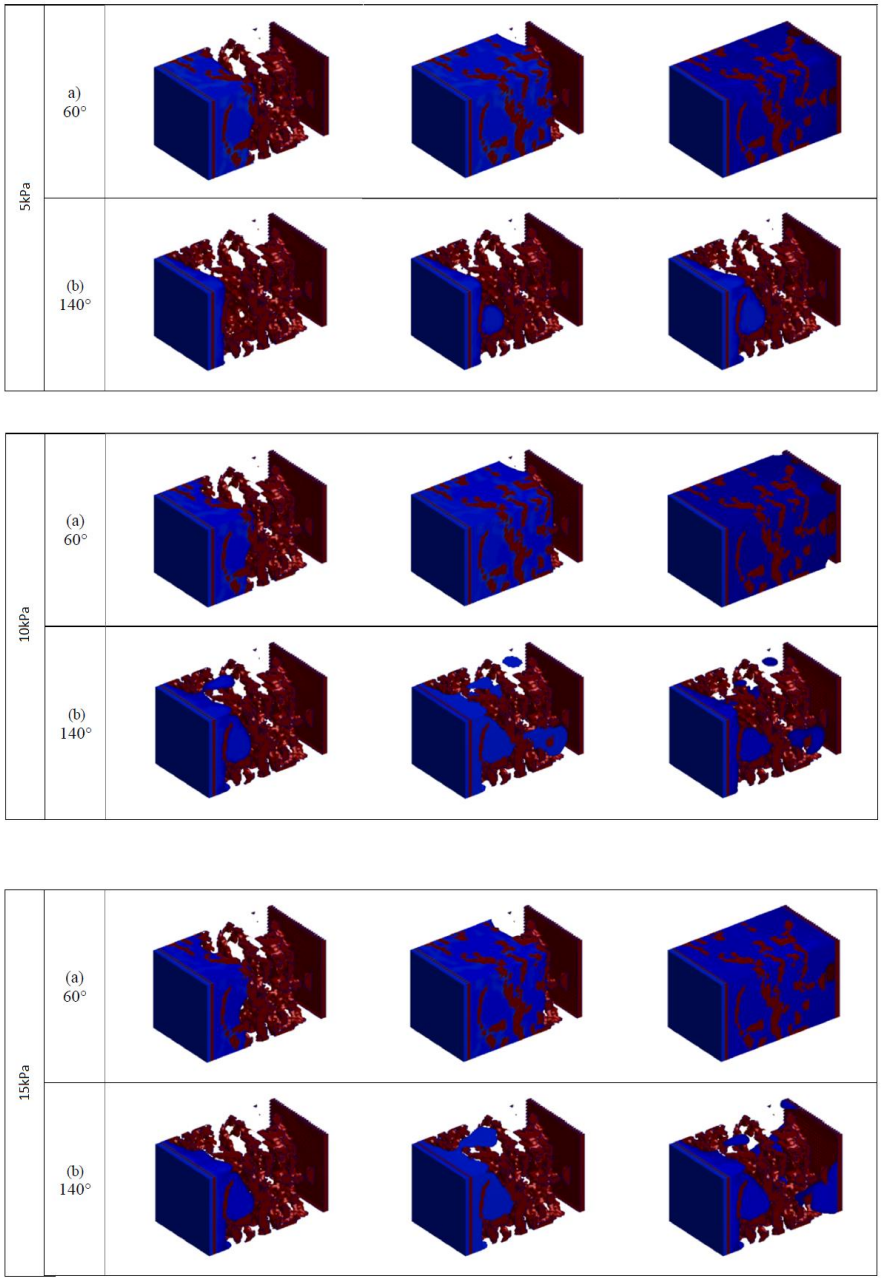

Figure 4 *- SGL paper intrusion patterns at contact angle of a) 60° b) 140° under 5 kPa, 10 kPa, and 15 kPa pressure differences*

4.1.1 Effects of GDL Wettability

As can be seen in **Figures 2-4**, the contact angles or wettability of each sample greatly determines the invasion pattern of liquid water through the samples. As the wettability changes from hydrophilic to hydrophobic, as determined by the contact angle change, the water invasion also

changes. For contact angles representing a hydrophilic sample, water displaces air in a uniform manner, with homogenous invasion properties. As the water passed through the sample, it saturates all pores with a flat invasion front. For more moderate contact angles and hydrophilic tendencies, capillary resistance force depends little on the pore size. Because of this, it is easy for the water to fill the pores, both large and small, resulting in the observed homogenous invasion front. This phenomenon is termed 'stable displacement'. This stable displacement was observed for all sample GDLs, and these results agree with the work in [34].

When the contact angles change to hydrophobic, water transport is no longer of stable displacement, and instead it passes through the structure partially saturating the domain, occupying certain voids in the GDL's porous network. This phenomenon is termed 'capillary fingering'. This observation is shared with [27,29,34].

The results in this study show that the transition between stable displacement and capillary fingering phenomena occurs abruptly, from $60°<\theta<90°$ to $100°<\theta<140°$. This does not agree with the work in [16] that shows the transition occurring at a contact angle of 90°. This study shows that the transition occurs in the region of $100°<\theta<120°$ in the case of the Freudenberg felt, and $90°<\theta<100°$ for the Toray paper. However, without further studies to evaluate smaller increments of contact angle, a precise angle cannot be confirmed.

4.1.2 Effects of GDL Structure

Although all sample GDLs showed capillary fingering at hydrophobic contact angles, the nature of this movement differs between samples. With the Freudenberg felt GDL, water entering the GDL forms convex water fronts because of the inherent hydrophobicity of the material. The liquid water penetrates the sample with a finger-like invasion pattern. The water selects some preferred pathways through the sample depending upon the local capillary resistance force.

In contrast to the Freudenberg felt, the Toray paper sample shows water travelling through the in-plane direction clearly. Liquid water enters from the front and travels selectively through large pores in the through-plane direction. However, at certain cross sections (at around 35% and 70% thickness) water then invades the in-plane direction and occupies all pores at that cross-section.

This difference highlights the difference in GDL construction between the two samples.

4.1.3 Effects of Applied Pressure Difference

Analysing the results of the differing pressures that the samples were subjected to shows that pressure difference has no effect on the intrusion pattern of liquid water. Although pressure difference has no effect on invasion pattern, the pressure does affect how far the water can penetrate through the sample.

All three samples showed the same stable displacement behaviours under hydrophilic contact angles for each pressure difference. At hydrophobic contact angles, capillary fingering behaviours were observed throughout the pressure range. The only exception being with the Freudenberg felt GLD at 5kPa pressure difference, which showed a stable displacement for all contact angles. This is attributed to the surface wettability and the resulting capillary resistance force where the contact angles (120^{o} and 140^{o}) create high capillary resistance, meaning that a higher pressure is needed for transformation. Our observations show that water travels only a very short distance before stopping at about 10% thickness. It is assumed that an increase in pressure difference above 5kPa allows capillary fingering to occur.

4.2 Water Saturation Distribution

Figures 5-7 show liquid water evolution through the three GDL structures at different times throughout the simulation. The water saturation distribution graph for the contact angle of 60^{o} is

first shown, with the most sever contact angle presented to the right (140^{o}) for each pressure difference (5kPa, 10kPa, 15kPa).

These figures offer the average cross-sectional saturation levels along the through-plane direction of each sample. This average is defined as the ratio of area occupied by liquid water to the overall void area in the given cross-section. Given this, the saturation level lies in the range of zero to one. Zero denoting the absence of water, and one showing a fully saturated region.

These figures confirm the observations from **Figures 2-4** in that the evolution of water distribution follows a stable displacement pattern to capillary fingering pattern from hydrophilic to hydrophobic contact angles.

Stable displacement patterns can be observed via the somewhat flat saturation front profile, confirming water occupying almost all of the voids in the GDL cross-section. Contrary to this, capillary fingering can be seen by the complex saturation profile with concaved shapes, confirming that water is only partially filling certain voids.

4.2.1 GDL With Felt Structure

The Freudenberg felt sample showed stable displacement at all contact angles at 5 kPa pressure difference. At the same pressure difference, the intrusion distance of water decreased with an increasing contact angle. Water passed through the sample thickness in all contact angles from hydrophilic to moderate (90^{o}). However, when these angles are increased a longer period of time is needed for breakthrough (from 98.96 ms at 60^{o} to 203.13 ms at 90^{o}). Water fails to pass through the GDL at 100^{o} angle and above.

At 10kPa differences in pressure, stable displacement is shown and breakthrough is shown up until 100^{o} contact angle. At angles of 120^{o}, water passed through the sample thickness with capillary fingering behaviour, with a substantial drop in saturation level. At 140^{o}, water is still travelling with

capillary fingering but saturation stops at around 40% thickness, as can be observed in **Figure 5b**. This saturation level is around 20% greater than the 5 kPa example (**Figure 5a**), showing how pressure difference influences water intrusion distance.

Increasing the pressure difference to 15 kPa shows the same behaviour as the previous pressure differences, however water breaks through in all cases.

Breakthrough time increased with contact angles, from 41.67 ms at 60^{o} to 109.38 ms at 140^{o}. This time is also increased by increasing pressure difference from 5-15 kPa.

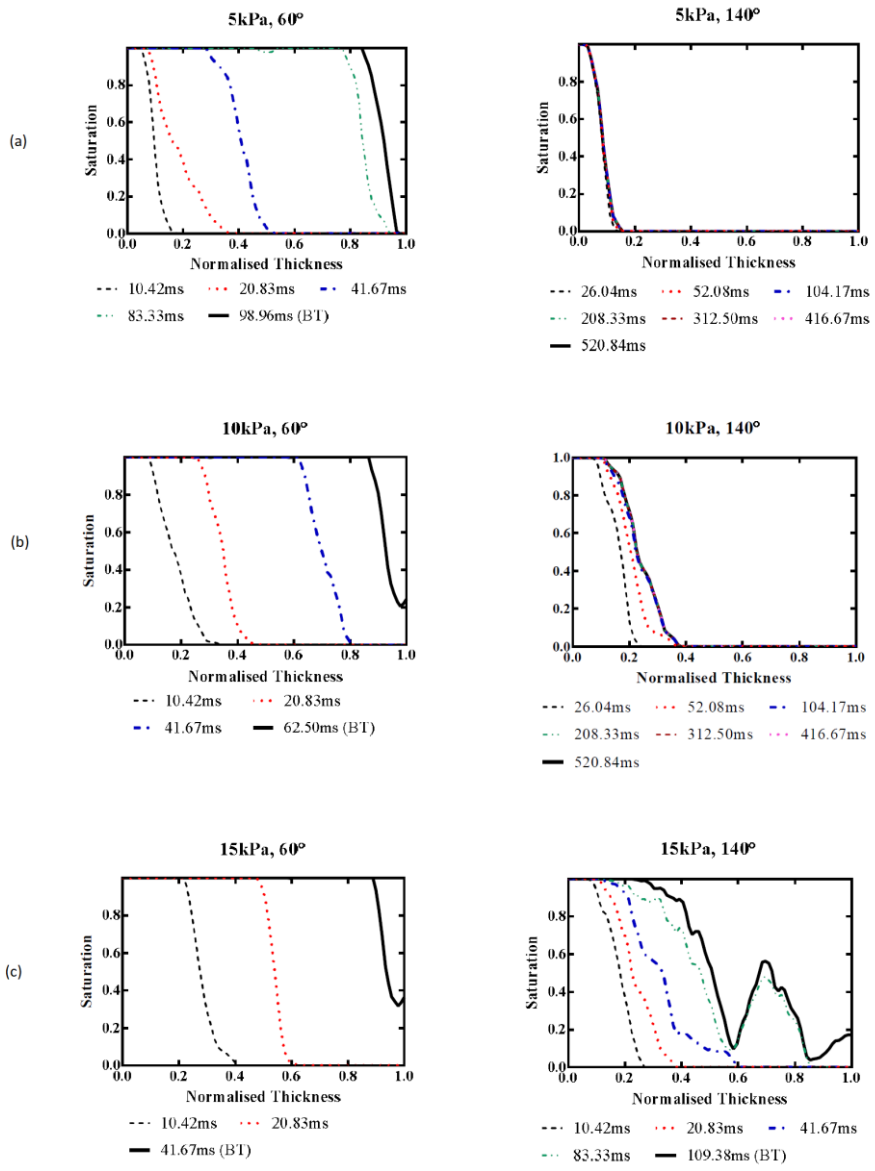

Figure 5 *- Water distributions across the thickness of the Freudenberg felt at 60° and 140° contact angles at the applied pressure difference of (a) 5 kPa, (b) 10 kPa, and (c) 15 kPa.*

4.2.2 GLD with paper structure

The Toray GDL paper showed stable displacement fronts at hydrophilic and moderate contact angles (until 100°), changing to capillary fingering at angles above 120°. With a pressure difference of 5 kPa no contact angles showed water breakthrough. Up until 100°, water can penetrate the GDL to around 60-70% thickness, whereas at higher contact angles (120°+) water stops at around 15-20% thickness.

Notably, at the contact angle of 100^{o} and 5kPa, stable displacement is observed, however small pockets of air are not displaced by water at 208.33 ms and 416.67 ms. These pockets of air are subsequently filled with water at later time-steps, showing early onset capillary fingering.

The same trends as above are shown in the 10 and 15 kPa runs. Under a pressure difference of 10 kPa at an angle of 100^{o} water front profiles show a large decrease in saturation in cross sections at 31.25 ms and 62.50 ms, with 20% of void spaces not occupied by water.

At 15 kPa at the same angle, stable displacement is shown with a flat front profile but small pockets are not filled with water until around 125 ms.

At angles of 120^{o} and 140^{o} under 10 kPa and 15 kPa, the sample thickness is fully saturated further down the thickness of the GDL, as seen in **Figure 6b** and **6c**. This behaviour differs from the Freudenberg sample, where once water saturation has dropped, it never recovers.

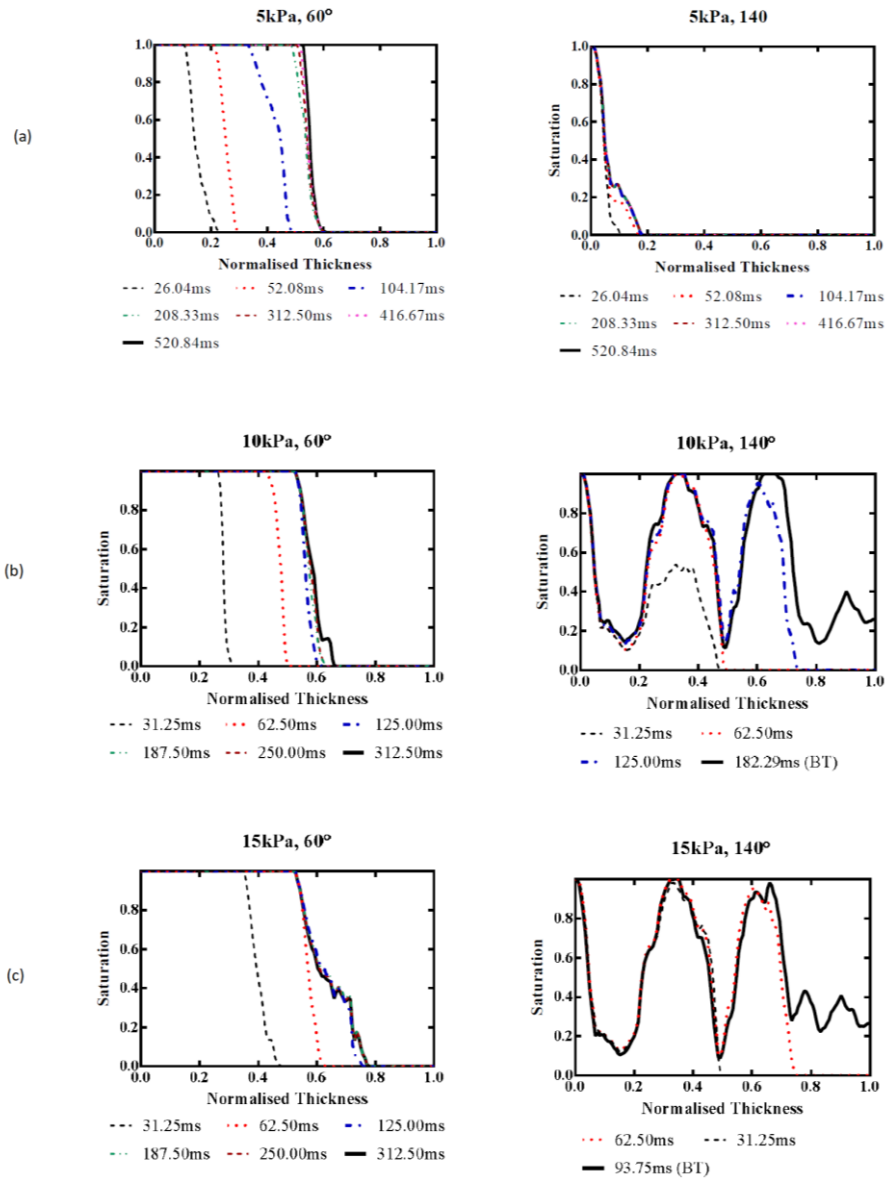

Figure 6 *- Water distributions across the thickness of the Toray paper at 60° and 140° contact angles at the applied pressure difference of (a) 5 kPa, (b) 10 kPa, and (c) 15 kPa.*

Additionally, unlike the Freudenberg GDL, the Toray paper at 10-15 kPa pressure differences shows breakthrough time decreases from 229.17 ms at 120° and 182.29 ms at 140° for 10 kPa, and 98.96 ms to 93.75 ms for the 15 kPa pressure difference. Again, the increased pressure difference of 10-15 kPa significantly decreases time to breakthrough, which is around 50% for both cases.

The SGL paper GDL material shows similar characteristics to the felt GDL material. Stable displacement is displayed at 5 kPa at hydrophilic angles, whereas capillary fingering is shown at hydrophobic angles. These patterns change at around 100^{o} contact angle, noted by a sudden drop in saturation at 156.25 ms in the 100^{o} case. Notably however, after the drop in saturation, saturation is regained as time moves on and the profile becomes flat and stable again.

Up until 120^{o} contact angle at 5 kPa water passes through the sample consistently and breaks through, with the time to breakthrough increasing from 104.17 ms at 60^{o} to 291.67 ms at 120^{o}. However at 140^{o} water does not break through the sample thickness, stopping at around 40% thickness. This suggests the contact angle's effects on breakthrough where higher contact angles create more capillary resistance and prohibit water passage.

10 kPa and 15 kPa pressures show a similar behaviour with stable displacement throughout hydrophilic angles and capillary fingering for hydrophobic angles (100^{o}+). Saturation figures also show increasing breakthrough time with increased pressure, from 62.50 ms at 60^{o} to 72.92 ms at 90^{o} for 10 kPa. For 15 kPa, the times increase from 41.67 ms at 60^{o} to 46.88 ms at 90^{o}. However conversely, the breakthrough time decreases in the hydrophobic region, with 78.13 ms at 100^{o} to 52.08 ms at 140^{o} at 10 kPa and 36.46 ms at 100^{o} to 26.04 ms at 140^{o}. This is similar behaviour to the Toray paper GDL.

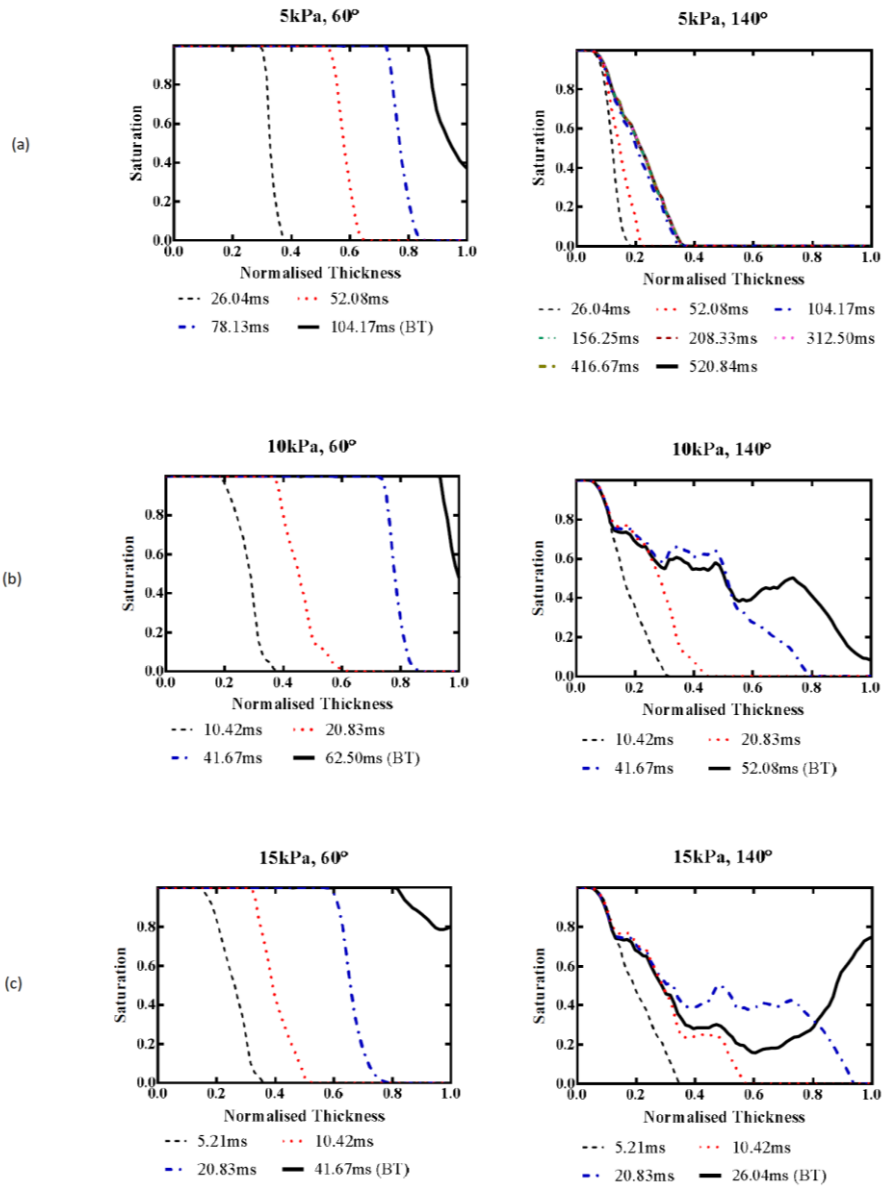

Figure 7 *- Water distributions across the thickness of the SGL paper at 60^{o} and 140^{o} contact angles at the applied pressure difference of (a) 5 kPa, (b) 10 kPa, and (c) 15 kPa*

4.3 Breakthrough Behaviour

Various similarities and differences can be drawn from the breakthrough characteristics of each GDL construction type. The Freudenberg felt experiences breakthrough at almost all contact angles, from hydrophilic, all the way through to hydrophobic. However, the Toray paper type GDL shows

breakthrough characteristics only in hydrophobic contact angles. SGL GDLs, as per the Freudenberg felt, experiences breakthrough at all contact angles.

The inherent construction of each sample shines some light on why this is the case. The Freudenberg felt has a 3D structure where the fibres travel in the through-plane and in-plane directions. In this case, there is no requirement for a binder material. The vast majority of its fibres run in the in-plane direction, allowing for local saturation. At hydrophilic contact angles, the through-plane fibres accommodate the adhesion of water to these fibres, leading to saturation through the thickness of the GDL, allowing stable displacement.

In contrast to this, the Toray paper has a 2D structure, with fibres only travelling in the in-plane direction. Therefore, a binding agent is required for structural integrity. In addition to reducing pore size and porosity of the material, the carbonized binder increases the contact area between solid surface and liquid water. This increased surface area of the binder would hold more water than if a binder was not used. This explains the layered saturation characteristics of this sample.

The SGL paper also uses a binder; however, it is a rough binder and not a layered type. This binder is spread over the fibres through the in-plan and through-plane directions, forming a 3D staircase-like structure. This allows the sample to draw in water to move into the sample domain in the thickness direction and then breakthrough at hydrophobic angles. This discovery shows that the binder in paper GDLs plays a significant role in water transport behaviour.

4.4 Breakthrough Saturation Levels

The point where water breaks through the outlet of each sample is shown in **Figure 8**. These breakthrough saturation levels were noted at each contact angle from 60^{o} to 140^{o} and under each pressure difference of 5-15 kPa.

4.4.1 Freudenberg Felt GDL

Figure 8a shows that at all three pressure differences showed similar saturation levels at breakthrough. At lower and intermediate contact angles saturation levels were around 100%, showing that water occupied all of most of the void spaces. Alternatively, these saturation levels decreased from full saturation at more hydrophilic contact angles, to partial saturation at intermediate to higher hydrophobic domains. Higher contact angles, in the region of 140^{o}, these levels reduce to around 62.5%.

This change in saturation levels from full to partial occurs in the region of 100^{o} and 120^{o}, with full saturation observed at 100^{o} but an 18.7% reduction in saturation at $120^{o,}$ confirming the influence of hydrophobicity on saturation in the felt GDL.

4.1.2 Toray paper GDL

As can be seen in Figure 8b, contact angles of 110^{o}, 115^{o}, and 130^{o} showed a decreasing trend in saturation levels. It was found that breakthrough only occurs under pressure differences of 10kPa and 15kPa, and at contact angles of 115^{o} and upwards. Saturation levels at breakthrough characteristics decrease as the contact angle increases.

For example, at 140^{o} with 15kPa pressure difference, the saturation level at breakthrough is 54.3%.

4.1.3 SGL paper GDL

Similar in respect to the Freudenberg felt GDL in that GDL wettability significantly affects saturation levels at breakthrough. Lower and intermediate contact angles show saturation levels at 100%, showing that water fills the entire GDL domain when water breaks through the material. With higher contact angles however, decreased saturation levels are observed. At angles of 140^{o} this drop is in the region of 39.2%. Figure 8c shows full saturation at 90^{o}, but at 100^{o} there is an 8.3% reduction in saturation, suggesting hydrophobicity's impact on saturation in SGL GDLs.

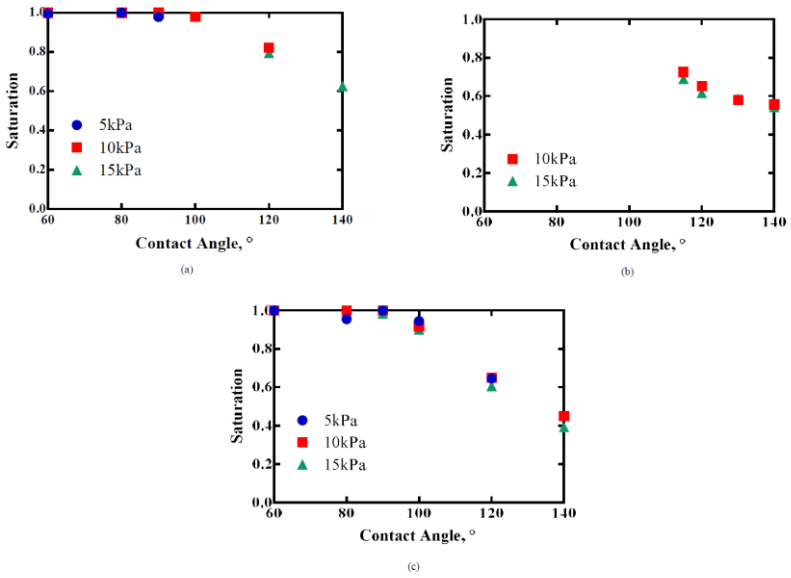

Figure 8 *- Water saturation levels at breakthrough for (a) Freudenberg felt (b) Toray paper (c) SGL paper*

For all three GDL samples, the results showed that a contact angle is the major deciding factor regarding saturation levels and breakthrough. The main observation being that at hydrophilic angles, water occupies all pores, whereas at hydrophobic angles, water only partially occupies pores, decreasing saturation and breakthrough.

At the angle of 140^{o}, the average saturation level of all three GDLs was 52%, showing that half of the GDL volume could facilitate gaseous flow. These results agree with the work in [14, 28-30], which suggested that the enhancement of hydrophobicity of the GDL will provide space for gaseous transport through the GDL material.

In terms of pressure difference, pressure differences that were applied across the thickness of the sample don't affect saturation levels at breakthrough. At all three pressure differences, all samples showed almost exactly the same saturation levels over the range of contact angles. Pressure difference does however, impact on breakthrough time.

5. Conclusions

This work presents the findings from an investigation into liquid water behaviour in PEMFC GDLs under varying wettability conditions and applied pressure differences. XCT reconstructed models of three types of commercial GDL were input to a two-phase LB model to determine the water's behaviour characteristics.

The work contained in this study observes water transport behaviour in uncompressed GDLs, with no PTFE or MPL applied. The results as such are comparable to ex-situ testing of GDL materials rather than actual invasion patterns in an operational PEMFC.

5.1 GDL Wettability effects

The water invasion pattern and the overall saturation level of liquid water in the GDL was heavily influenced by the material wettability (contact angle). Stable displacement was observed in all GDLs with hydrophilic contact angles, whereas capillary fingering was observed in hydrophobic GDLs. Saturation levels decreased in the region of 50% in highly hydrophobic GDLs, which left 50% of the pores available for gas transport. The transition between the two phenomena occurred between 90^{o} and 120^{o}.

5.2 Applied Pressure effects

Breakthrough was partially controlled by GDL wettability, with higher pressure differences influencing breakthrough at high contact angles. Generally speaking, liquid water broke through the entire sample thickness at 10kPa and 15kPa pressure differences. However, at 5kPa breakthrough rarely occurred. This suggests that a 5kPa difference in pressure is insufficient to encourage water breakthrough.

Regarding invasion patterns and saturation levels under these conditions, differing applied pressures showed no influence on either aspect.

When assessing the water saturation figures above, it is clear that all three applied pressure difference showcase the same trend. The GDL samples become fully saturated at hydrophilic contact angles and partially saturated at hydrophobic angles.

5.3 GDL Structure effects

Regarding invasion patterns, all three GDL samples studied showed differences in capillary fingering in the hydrophobic case. In the felt sample, liquid water invaded mainly in the through-plane direction, whereas the paper with a 2D binder showed invasion in the in-plane direction. For the paper GDL with a 3D binder, invasion patterns were observed in both the through and in-plane directions.

Additionally, the structure of each GDL proved to heavily influence the water breakthrough characteristics. This difference in breakthrough nature is due to the number of through-plane fibres in the felt GDL rather than paper. Through-plane fibres favour water transport at hydrophilic contact angles when water interaction is adhesive in nature. The paper GDL with a 3D binder also showed through-plane fibres as with the felt, both leading to water travel in the same direction. However, the 2D bound paper GDL contains mainly in-plane fibres, and thus, liquid water would attach to these fibres, and move along in the in-plane direction.

GDL structure was found to have negligible breakthrough influence with hydrophobic GDL materials. On the other hand, each GDL material contributed to a significant difference in the capillary fingering behaviour when under hydrophobic contact angles.

6. Acknowledgement

The authors would like to gratefully acknowledge The Royal Thai Government Scholarship for funding the PhD research study of Fontip Jinuntuya and the UK Department of Trade and Industry

(DTI) and Engineering and Physical Sciences Research Council (EPSRC) for funding this research work under Grant Number: TP/6/DAM/6/S/K3032H.

7. References

[1] Bazylak, A., Liquid water visualization in PEM fuel cells: A review. International Journal of Hydrogen Energy, 2009. 34(9): p. 3845-3857.

[2] Litster, S., D. Sinton, and N. Djilali, Ex situ visualization of liquid water transport in PEM fuel cell gas diffusion layers. Journal of Power Sources, 2006. 154(1): p. 95-105.

[3] Bazylak, A., et al., Effect of compression on liquid water transport and microstructure of PEMFC gas diffusion layers. Journal of Power Sources, 2007. 163(2): p. 784-792.

[4] Pasaogullari, U. and C.Y. Wang, Liquid water transport in gas diffusion layer of polymer electrolyte fuel cells. Journal of the Electrochemical Society, 2004. 151(3): p. A399-A406.

[5] Nam, J.H. and M. Kaviany, Effective diffusivity and water-saturation distribution in single- and two-layer PEMFC diffusion medium. International Journal of Heat and Mass Transfer, 2003. 46(24): p. 4595-4611.

[6] Natarajan, D. and T. Van Nguyen, A Two-Dimensional, Two-Phase, Multicomponent, Transient Model for the Cathode of a Proton Exchange Membrane Fuel Cell Using Conventional Gas Distributors. Journal of The Electrochemical Society, 2001. 148(12): p. A1324-A1335.

[7] Siegel, N.P., et al., A two-dimensional computational model of a PEMFC with liquid water transport. Journal of Power Sources, 2004. 128(2): p. 173-184.

[8] Wang, Z.H., C.Y. Wang, and K.S. Chen, Two-phase flow and transport in the air cathode of proton exchange membrane fuel cells. Journal of Power Sources, 2001. 94(1): p. 40-50.

[9] You, L.X. and H.T. Liu, A two-phase flow and transport model for the cathode of PEM fuel cells. International Journal of Heat and Mass Transfer, 2002. 45(11): p. 2277-2287.

[10] Wang, Y. and C.Y. Wang, A non-isothermal, two-phase model for polymer electrolyte fuel cells. Journal of the Electrochemical Society, 2006. 153(6): p. A1193-A1200.

[11] Mukherjee, P.P., Q.J. Kang, and C.Y. Wang, Pore-scale modeling of two-phase transport in polymer electrolyte fuel cells-progress and perspective. Energy & Environmental Science, 2011. 4(2): p. 346-369.

[12] Jiao, K. and X. Li, Water transport in polymer electrolyte membrane fuel cells. Progress in Energy and Combustion Science, 2011. 37(3): p. 221-291.

[13] Wang, Y., et al., A review of polymer electrolyte membrane fuel cells: Technology, applications, and needs on fundamental research. Applied Energy, 2011. 88(4): p. 981-1007.

[14] Chapuis, O., et al., Two-phase flow and evaporation in model fibrous media Application to the gas diffusion layer of PEM fuel cells. Journal of Power Sources, 2008. 178(1): p. 258-268.

[15] Hinebaugh, J., Z. Fishman, and A. Bazylak, Unstructured Pore Network Modeling with Heterogeneous PEMFC GDL Porosity Distributions. Journal of The Electrochemical Society, 2010. 157(11): p. B1651-B1657.

[16] Chraibi, H., et al., Influence of wettability on liquid water transport in gas diffusion layer of proton exchange membrane fuel cells (PEMFC). arXiv preprint arXiv:0909.2947, 2009.

[17] Hinebaugh, J. and A. Bazylak, Condensation in PEM Fuel Cell Gas Diffusion Layers: A Pore Network Modeling Approach. Journal of The Electrochemical Society, 2010. 157(10): p. B1382-B1390.

[18] Medici, E.F. and J.S. Allen, The Effects of Morphological and Wetting Properties of Porous Transport Layers on Water Movement in PEM Fuel Cells. Journal of the Electrochemical Society, 2010. 157(10): p. B1505-B1514.

[19] Sinha, P.K. and C.Y. Wang, Liquid water transport in a mixed-wet gas diffusion layer of a polymer electrolyte fuel cell. Chemical Engineering Science, 2008. 63(4): p. 1081-1091.

[20] Sinha, P.K. and C.Y. Wang, Pore-network modeling of liquid water transport in gas diffusion layer of a polymer electrolyte fuel cell. Electrochimica Acta, 2007. 52(28): p. 7936-7945.

[21] Hinebaugh, J. and A. Bazylak. PEM Fuel Cell Gas Diffusion Layer Modelling of Pore Structure and Predicted Liquid Water Saturation. in ASME 2011 9th International Conference on Fuel Cell Science, Engineering and Technology collocated with ASME 2011 5th International Conference on Energy Sustainability. 2011. American Society of Mechanical Engineers.

[22] Lee, K.J., J.H. Nam, and C.J. Kim, Pore-network analysis of two-phase water transport in gas diffusion layers of polymer electrolyte membrane fuel cells. Electrochimica Acta, 2009. 54(4): p. 1166-1176.

[23] Lee, K.J., J.H. Nam, and C.J. Kim, Steady saturation distribution in hydrophobic gas-diffusion layers of polymer electrolyte membrane fuel cells: A pore-network study. Journal of Power Sources, 2010. 195(1): p. 130-141.

[24] Rama, P., et al., An X-Ray Tomography Based Lattice Boltzmann Simulation Study on Gas Diffusion Layers of Polymer Electrolyte Fuel Cells. Journal of Fuel Cell Science and Technology, 2010. 7(3): p. 031015-031015.

[25] Mukherjee, P.P., et al., Numerical Modeling of Two-Phase Behavior in the PEFC Gas Diffusion Layer. ECS Transactions, 2010. 26(1): p. 97-106.

[26] Koido, T., T. Furusawa, and K. Moriyama, An approach to modeling two-phase transport in the gas diffusion layer of a proton exchange membrane fuel cell. Journal of Power Sources, 2008. 175(1): p. 127-136.

[27] Mukherjee, P.P., C.-Y. Wang, and Q. Kang, Mesoscopic modeling of two-phase behavior and flooding phenomena in polymer electrolyte fuel cells. Electrochimica Acta, 2009. 54(27): p. 6861-6875.

[28] Rama, P., et al., Simulation of liquid water breakthrough in a nanotomography reconstruction of a carbon paper gas-diffusion layer. AIChE Journal, 2012. 58(2): p. 646-655.

[29] Gao, Y., et al., Lattice Boltzmann simulation of water and gas flow in porous gas diffusion layers in fuel cells reconstructed from micro-tomography. Computers & Mathematics with Applications, 2013. 65(6): p. 891-900.

[30] Rama, P., et al., A Numerical Study of Structural Change and Anisotropic Permeability in Compressed Carbon Cloth Polymer Electrolyte Fuel Cell Gas Diffusion Layers. Fuel Cells, 2011. 11(2): p. 274-285.

[31] Rama, P., et al., Multiscale Modeling of Single-Phase Multicomponent Transport in the Cathode Gas Diffusion Layer of a Polymer Electrolyte Fuel Cell. Energy & Fuels, 2010. 24(5): p. 3130-3143.

[32] Shan, X.W. and H.D. Chen, Lattice Boltzmann Model for Simulating Flows with Multiple Phases and Components. Physical Review E, 1993. 47(3): p. 1815- 1819.

[33] Shan, X.W. and H.D. Chen, Simulation of Nonideal Gases and Liquid-Gas Phase-Transitions by the Lattice Boltzmann-Equation. Physical Review E, 1994. 49(4): p. 2941-2948.

[34] Hao, L. and P. Cheng, Lattice Boltzmann simulations of water transport in gas diffusion layer of a polymer electrolyte membrane fuel cell. Journal of Power Sources, 2010. 195(12): p. 3870-3881.